Importin binding mediates the intramolecular regulation of anillin during cytokinesis

Daniel Beaudet[a], Nhat Pham[b], Noha Skaik[b], and Alisa Piekny[b,*]
[a]Department of Bioengineering, McGill University, Montreal, QC, Canada, H3A 0G4; [b]Department of Biology, Concordia University, Montreal, QC, Canada, H4B 1R6

ABSTRACT **Cytokinesis occurs by the ingression of an actomyosin ring that cleaves a cell into two daughters. This process is tightly controlled to avoid aneuploidy, and we previously showed that active Ran coordinates ring positioning with chromatin. Active Ran is high around chromatin, and forms an inverse gradient to cargo-bound importins. We found that the ring component anillin contains a nuclear localization signal (NLS) that binds to importin and is required for its function during cytokinesis. Here we reveal the mechanism whereby importin binding favors a conformation required for anillin's recruitment to the equatorial cortex. Active RhoA binds to the RhoA-binding domain causing an increase in accessibility of the nearby C2 domain containing the NLS. Importin binding subsequently stabilizes a conformation that favors interactions for cortical recruitment. In addition to revealing a novel mechanism for the importin-mediated regulation of a cortical protein, we also show how importin binding positively regulates protein function.**

Monitoring Editor
Fred Chang
University of California, San Francisco

Received: Jan 6, 2020
Revised: Mar 24, 2020
Accepted: Mar 25, 2020

INTRODUCTION

Cytokinesis occurs at the end of mitosis to physically separate a cell into two daughters. This process must be strictly controlled to ensure that each daughter inherits the appropriate genetic material and cell fate determinants. Cytokinesis occurs due to the ingression of an actomyosin ring (Green *et al.*, 2012). Contractile proteins localize broadly around the cortex in early anaphase and are restricted to the equatorial zone before furrow ingression. Ring assembly and ingression is regulated by active RhoA, which binds to effectors that regulate F-actin and activate nonmuscle myosin II (Piekny *et al.*, 2005, Basant and Glotzer, 2018). Active RhoA also recruits the scaffold protein anillin, which cross-links the actomyosin ring to the plasma membrane and feeds back to stabilize active RhoA for robust cytokinesis (Piekny and Glotzer, 2008; van Oostende Triplet *et al.*, 2014; Sun *et al.*, 2015; Budnar *et al.*, 2019). Because anillin cross-links key components of the cell during cytokinesis, understanding its molecular regulation can provide insight into how cytokinesis is regulated. In particular, the C-terminus of anillin contains a RhoA-GTP binding domain (RBD), a neighboring C2 domain, and a pleckstrin homology (PH) domain, which coordinate its localization through 1) binding to active RhoA, 2) binding to phospholipids, importins, and/or microtubules via the C2 domain, and 3) binding to phospholipids and/or septins via the PH domain (Oegema *et al.*, 2000; Piekny and Glotzer, 2008; Piekny and Maddox, 2010; Liu *et al.*, 2012; van Oostende Triplet *et al.*, 2014; Sun *et al.*, 2015; Beaudet *et al.*, 2017). However, which of these interactions is crucial for anillin function and how they are coordinated is not clear.

Multiple mechanisms regulate cytokinesis and are derived from spindle-dependent (e.g., Dechant and Glotzer, 2003; Somers and Saint, 2003; Bement *et al.*, 2005; Bringmann and Hyman, 2005; Yüce *et al.*, 2005; Zhao and Fang, 2005; Werner *et al.*, 2007; Lewellyn *et al.*, 2010; van Oostende Triplet *et al.*, 2014; Pollard and O'Shaughnessy, 2019) and -independent pathways (e.g., von Dassow *et al.*, 2009; Cabernard *et al.*, 2010; Schenk *et al.*, 2010; Sedzinski *et al.*, 2011; Kiyomitsu and Cheeseman, 2013; Zanin *et al.*, 2013; Rodrigues *et al.*, 2015; Beaudet *et al.*, 2017). The central spindle forms between segregating chromosomes during anaphase and contains anti-parallel bundled microtubules. Centralspindlin, a

This article was published online ahead of print in MBoC in Press (http://www.molbiolcell.org/cgi/doi/10.1091/mbc.E20-01-0006) on April 2, 2020.

A.P. and D.B. wrote the original manuscript and conceptualized and designed the methodology for experiments. D.B., N.P., and N.S. performed the experiments and analyzed the data. D.B. made the data into figures for visualization. Funds were acquired by A.P. Supervision was carried out by A.P. and D.B.

*Address correspondence to: Alisa Piekny (alisa.piekny@concordia.ca).

Abbreviations used: FRAP, fluorescence recovery after photobleaching; GEF, guanine nucleotide exchange factor; GST, Glutathione *S*-transferase; I/F, interface; MBP, maltose-binding protein; NLS, nuclear localization signal; O/E, overexpression; PH, pleckstrin homology; RBD, Rho-binding domain; RNAi, RNA interference.

heterotetramer of Cyk-4 and MKLP1, bundles central spindle microtubules and forms a complex with the RhoA guanine nucleotide exchange factor (GEF) Ect2, which stimulates the activation of RhoA in the equatorial cortex (Mishima *et al.*, 2002, 2004; Bement *et al.*, 2005; Yüce *et al.*, 2005; Petronczki *et al.*, 2007; Burkard *et al.*, 2009; Wolfe *et al.*, 2009). Several studies showed that the membrane localization of this complex is crucial for Ect2's GEF activity versus spindle localization and the role of microtubules remains to be clarified (Frenette *et al.*, 2012; Lakomtsev *et al.*, 2012; Basant *et al.*, 2015; Kotýnková *et al.*, 2016). Astral microtubules emanate toward the poles and inhibit contractility at the nearby cortex. Cells treated with nocodazole to depolymerize microtubules cause a global increase in active RhoA and an increase in the breadth of accumulated contractile proteins (Chang *et al.*, 2008; Murthy and Wadsworth, 2008; Zanin *et al.*, 2013; van Oostende Triplet *et al.*, 2014). Increasing the density of astral microtubules by depleting MCAK (a microtubule depolymerase) decreases the zone of accumulated contractile proteins, which is restored upon codepletion of anillin (Rankin and Wordeman, 2010; Zanin *et al.*, 2013; van Oostende Triplet *et al.*, 2014). Anillin directly binds to microtubules, and its localization to microtubules in cells is enhanced by increased microtubule stability or density, and decreased by active RhoA (Tse *et al.*, 2011; van Oostende Triplet *et al.*, 2014). Thus, astral microtubules may sequester anillin at the cell poles but not at the furrow to prevent contractility at the polar cortex (Tse *et al.*, 2011; van Oostende Triplet *et al.*, 2014). A recent study showed that in the early *Caenorhabditis elegans* embryo, the clearing of F-actin and anillin at the polar cortex depends on the astral microtubule-based TPXL-1-mediated activation of Aurora A kinase (Mangal *et al.*, 2018). However, it is unclear whether Aurora A activity directly impacts RhoA and/or anillin localization or whether there are other proteins involved because few other molecular regulators of the astral pathway are known (Bringmann *et al.*, 2007; Basant and Glotzer, 2018).

Chromatin sensing is one of the microtubule-independent mechanisms that regulates cytokinesis. Importins bind to the nuclear localization signals (NLS) on cargo to mediate their nuclear transport (Soniat and Chook, 2015). Active Ran is enriched in the nucleus and competes with importins to release cargo. During mitosis, the Ran gradient persists around chromatin where it controls spindle assembly (Li and Zheng, 2004; Kaláb *et al.*, 2006; Clarke and Zhang, 2008; Kaláb and Heald, 2008). The dogma is that importin binding to the NLS of a spindle regulator sterically blocks interactions with partners required for their function (Weaver and Walczak, 2015). Thus, active complexes assemble the spindle near chromatin where active Ran is high. However, findings from our lab and others suggests that cortical proteins could be regulated differently by importin binding (Deng *et al.*, 2007; Dehapiot *et al.*, 2013; Dehapiot and Halet, 2013; Samwer *et al.*, 2013; Kiyomitsu and Cheeseman, 2013; Beaudet *et al.*, 2017). In particular, importins function as a ruler during meiosis or cytokinesis where optimal levels facilitate polarization of the nearby cortex (Deng *et al.*, 2007; Silverman-Gavrila *et al.*, 2008; Dehapiot and Halet, 2013; Dehapiot *et al.*, 2013; Samwer *et al.*, 2013; Beaudet *et al.*, 2017). Ideal levels of importins could differ depending on the protein, and would be determined by the different affinities a cortical protein has for importin binding versus other interactors. For example, as shown by our group and the Wilde lab, if importins are too high they outcompete and prevent crucial interactions required for cortical recruitment (Silverman-Gavrila *et al.*, 2008; Beaudet *et al.*, 2017). This elegant system would control the localization of cortical proteins in response to chromatin position to ensure that the polar body or contractile ring is properly positioned. A recent study showed that importin-α is lipid-modified by palmitoylation in *Xenopus* egg extracts, and the authors proposed this creates a cortical sink of importin-α to reduce cytoplasmic levels for scaling spindle and nuclear size (Brownlee and Heald, 2019). It will be interesting to determine whether Palmitoylated importin-α can form functional complexes and mediate processes at the membrane.

Here we provide mechanistic insight into how importins regulate anillin. Previously, we found the C-terminal NLS of anillin is required for its localization and function during cytokinesis (Beaudet *et al.*, 2017). In addition, we found that the RBD autoinhibits the adjacent NLS-containing C2 domain. We proposed a model where binding to active RhoA facilitates a conformational change in anillin that increases accessibility to the C2 domain, and importin binding stabilizes this conformation to facilitate anillin's recruitment to the equatorial cortex. Here, we describe data supporting this model. Through fluorescence recovery after photobleaching (FRAP) experiments we found that mutating the NLS alters anillin's cortical dynamics. We also found that increasing active RhoA facilitates importin binding, while inactive RhoA or mutating the RBD decreases importin binding. Strikingly, anillin's localization and function are abolished when NLS mutations are combined with additional point mutations in the C2 domain that weaken its interface with the RBD. Anillin localization and function was similarly abolished with point mutations that more strongly disrupt the interface and cause anillin to bind more strongly to importin. Thus, the relative position of the RBD and C2 is essential for anillin's cortical recruitment, but also for ensuring that importin can be outcompeted by phospholipids and/or other cortical components.

RESULTS

The C-terminus has different cortical enrichment dynamics compared with full-length anillin

Anillin requires active RhoA for its recruitment to the equatorial cortex, but also relies on other interactions for its robust enrichment in the equatorial plane (Piekny and Glotzer, 2008; Sun *et al.*, 2015; Wagner and Glotzer, 2016). The C-terminus of anillin contains multiple binding domains including a RhoA-GTP–binding domain (RBD), a C2 domain with an NLS and binding sites for phospholipids, microtubules, and Ect2, and a PH domain that binds to phospholipids and septins (Figure 1A; Oegema *et al.*, 2000; Piekny and Maddox, 2010; Frenette *et al.*, 2012; Liu *et al.*, 2012; van Oostende Triplet *et al.*, 2014; Sun *et al.*, 2015). The C-terminus is sufficient for anillin's cortical enrichment and is now being used as a reporter for active RhoA (Piekny and Glotzer, 2008; Sun *et al.*, 2015; Wagner and Glotzer, 2016). However, we do not fully understand how interactions in the C-terminus are coordinated for anillin's localization and function.

To characterize the cortical dynamics of anillin, we performed fluorescence recovery after photobleaching (FRAP) experiments on HeLa cells expressing GFP-tagged full-length anillin and coexpressing mCherry:tubulin using equatorially positioned cortical regions of interest (ROIs). The percentage of fluorescence recovery was determined by measuring the fluorescence signal of the photobleached ROI relative to the prebleached ROI for 50 s at 2-s intervals. The bleached ROIs were corrected for background and photobleaching during image acquisition by subtracting background levels and internally controlling each experiment with a reference ROI on the opposite side of the cortex (Figure 1A). First, we compared anillin's cortical retention during early versus late ingression (Supplemental Figure S1). The stage of ingression was determined by the ratio of the length of the ingressed cortex over the width of the cell at the

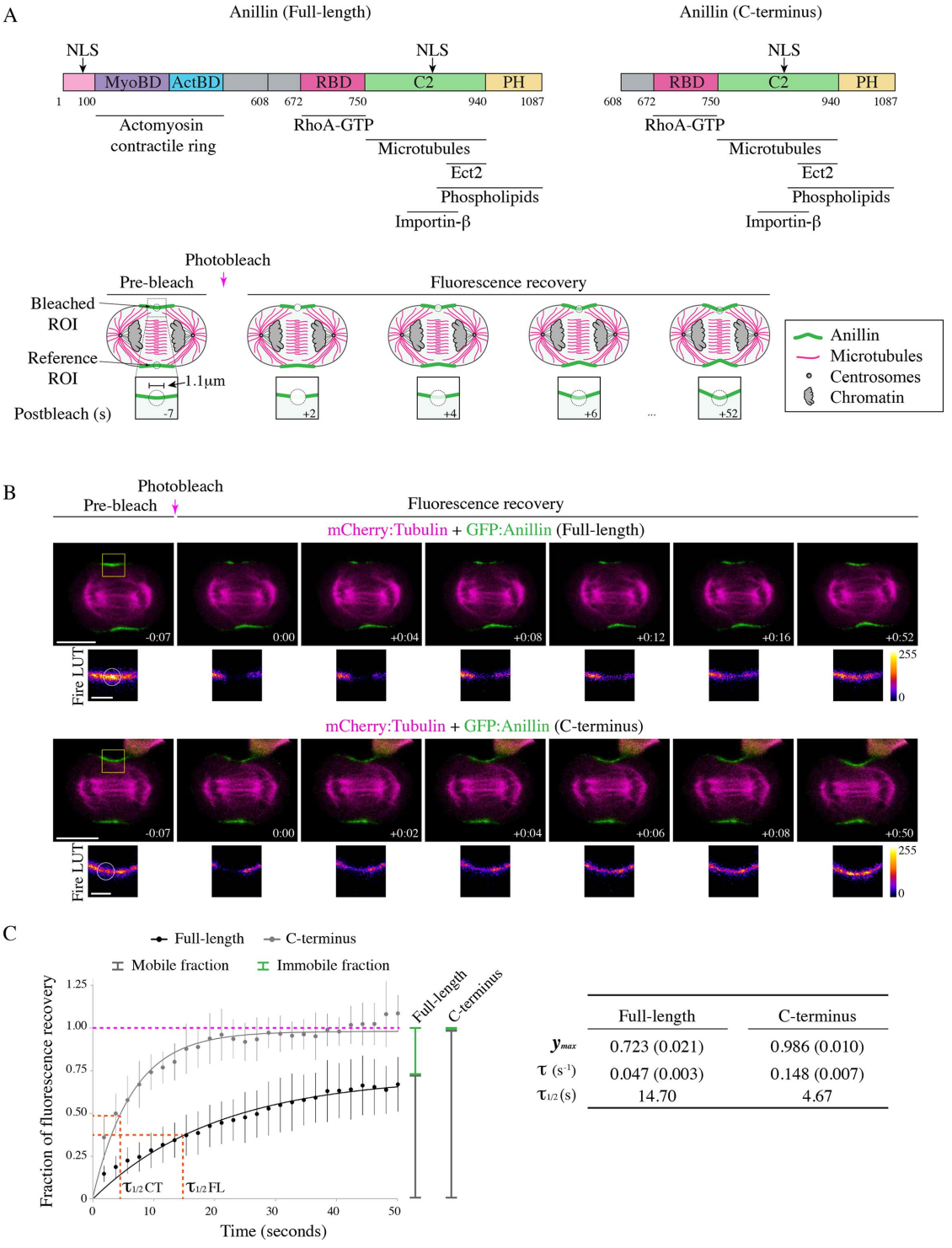

	Full-length	C-terminus
y_{max}	0.723 (0.021)	0.986 (0.010)
τ (s^{-1})	0.047 (0.003)	0.148 (0.007)
$\tau_{1/2}$ (s)	14.70	4.67

FIGURE 1: The C-terminus has different cortical dynamics compared with full-length anillin. (A) The structures of full-length and C-terminus of anillin are shown with binding domains as indicated (pink = contains N-terminal NLS; purple = MyoBD, binds myosin; blue = ActBD binds actin; magenta = RhoA-GTP binding domain [RBD], binds active RhoA; green = C2 domain, binds microtubules, phospholipids, Ect2, and contains C-terminal NLS that binds importin-β; yellow = pleckstrin homology [PH], binds phospholipids). Cartoon schematics show the fluorescence recovery after photobleaching (FRAP) of a region of interest (ROI) compared with a reference ROI in a cell expressing anillin (green) during anaphase and early ingression. The photobleached region is shown in the boxed inset. Other components of the cell are indicated in the legend (microtubules in magenta, centrosomes in gray, and chromatin in light-gray). (B) Time-lapse images show FRAP of HeLa cells expressing mCherry:tubulin (magenta) and GFP-tagged full-length (green; top panels) or C-terminus of anillin (green; bottom panels). The boxed insets show the ROIs that were photobleached in Fire look-up tables (LUTs). The scale bars are 10 or 2 µm for boxed insets. Indicated times are before (–) or after (+) photobleaching. (C) A graph shows the fraction of fluorescence recovery over time for full-length

equator, where $R > 0.6$ was "early" and $R < 0.6$ was "late" (Supplemental Figure S1A). There were no significant differences in the fluorescence recovery time constant (τ) between early and late ingression; however, there was an increase in the immobile fraction during late ingression (Supplemental Figure S1, B and C). This suggests that anillin has stronger cortical retention during late cytokinesis, which may be important for the contractile ring–midbody transition (El-Amine *et al.*, 2013, 2019).

Next, we determined how cortical dynamics differ between full-length anillin and the C-terminus (Figure 1B). As shown in the table, full-length anillin has greater cortical retention and a slower τ compared with the C-terminus (Figure 1C). The average τ for full-length anillin was 0.047 s^{-1} and recovered to a maximum of 72.3% of the prebleached intensity compared with the C-terminus, which had an average τ of 0.148 s^{-1} and recovered to 98.6% of the prebleached intensity (Figure 1C). The faster time constant and higher recovery suggests that the C-terminus is more mobile and has lower cortical retention compared with full-length anillin. This difference in mobility likely reflects interactions with more stable actomyosin filaments at the N-terminus versus active RhoA at the C-terminus, which also has high mobility and recovery (Budnar *et al.*, 2019; Piekny, unpublished observations).

The C-terminal NLS regulates anillin's cortical affinity during cytokinesis

Human anillin contains two well-characterized, functionally divergent NLS. The N-terminus contains a proline–tyrosine NLS that interacts with importin-β2 and functions to sequester anillin to the nucleus to prevent cytosolic accumulation of the protein that would otherwise have a drastic impact on cellular architecture during interphase (Chen *et al.*, 2015). Whereas, the C-terminal NLS matches the consensus sequence of a classic bipartite NLS and interacts with importin-β, which is required for cytokinesis (Beaudet *et al.*, 2017). We previously showed that mutating the NLS in the C-terminus of anillin causes both a delay in recruitment and a decrease in its breadth during cytokinesis (Figures 4 and 5, later in the paper; Beaudet *et al.*, 2017). This presumably occurs due to a decrease in importin binding, and to show this we performed in vitro binding studies (Figure 2A). Indeed, purified Glutathione *S*-transferase-tagged importin-β (GST:importin-β) bound to MBP:anillin (C2 domain), which was significantly reduced when the NLS was mutated (850KK851–DE, or 887KK888–DE in the longer isoform; Figure 2A and Supplemental Figure S2A). There are two isoforms of human anillin; one is 37 amino acids shorter (1–1087) than the other (1–1124) due to alternative splicing of a small exon (Piekny and Glotzer, 2008). Because our experiments were performed using the shorter isoform, we indicate what each mutation corresponds to in the longer isoform. To determine how the C-terminal NLS regulates anillin's cortical dynamics, we performed FRAP as described earlier. HeLa cells coexpressing mCherry:tubulin and GFP-tagged C-terminus of anillin containing the NLS mutations were measured during early ingression (Figure 2B). Mutating the NLS caused a decrease in the mobile fraction and a faster recovery time constant compared with the control. For example, the NLS mutant had an average τ of 0.323 s^{-1} and recovered to 73.6% of the prebleached signal intensity compared with control, which had an average τ of 0.148 s^{-1} and recovered to 98.6% of the prebleached signal intensity (Figure 2, B and C). These data suggest that importin binding to the NLS improves anillin's retention by reducing dissociation, but also makes anillin more dynamic in its ability to exchange with the cortex.

Astral microtubules also regulate the localization of anillin during cytokinesis. We previously showed that overextending the astral microtubules with MCAK RNAi caused a delay in anillin's cortical recruitment and localization to a narrow region of the equatorial cortex similar to the NLS mutant (Figure 2B; van Oostende Triplet *et al.*, 2014). We also found that disrupting the astral microtubules causes NLS mutant anillin to spread along the equatorial cortex (Beaudet *et al.*, 2017). Next, we determined how microtubules influence anillin's cortical turnover and retention by performing FRAP on HeLa cells coexpressing mCherry:tubulin and GFP-tagged C-terminus of anillin after MCAK RNAi (Figure 2, B and C). MCAK-depleted cells had an average τ of 0.167 s^{-1} and the fluorescence signal recovered to 77.2% of the prebleached signal (Figure 2C). Thus, astral microtubules decrease the mobility of cortical anillin, but have no impact on the recovery time. This suggests that the NLS mutant alters a cortical property of anillin independent of microtubules.

We previously found that the microtubule-binding region of anillin maps to the C2 domain, but the precise binding site was not determined (van Oostende Triplet *et al.*, 2014; Beaudet *et al.*, 2017). We wanted to determine whether the importin and microtubule binding regions overlap, and whether their binding is competitive. First, we performed cosedimentation assays to test how mutating the NLS changes anillin's affinity for microtubules. This was done using 1 μM of recombinant MBP-tagged C2 domain of control or NLS mutant anillin with varying concentrations of polymerized Taxol-stabilized microtubules (0.5–4 μM) and quantifying the amount of protein in the pellets versus supernatants on a Coomassie-stained gel (Supplemental Figure S2B). Anillin's affinity for microtubules was quantified by comparing bound (pellet) versus unbound (supernatant) protein, and was found to be 0.09 μM for control anillin compared with 0.96 μM for NLS mutant anillin (Supplemental Figure S2B). This ~10-fold decrease in affinity suggests that the NLS is partially required for microtubule binding. Next, we determined whether importin competes with microtubules for anillin binding. To test this, we performed cosedimentation assays using a fixed 1:2.5 μM ratio of anillin (MBP:anillin C2) and microtubules, and titrated in varying concentrations of recombinant GST:importin-β (0.2–1.5 μM; Supplemental Figure S2C). Increasing the concentration of importin-β reduced, but did not eliminate anillin binding to microtubules (Supplemental Figure S2C). Although these data suggest that importin and microtubules partially compete for anillin binding at a site that includes the NLS, there is a possibility that the affinity tags on either recombinant protein interfere with the ability to achieve a complete loss of microtubule binding with increased levels of importin. Thus, when the NLS is mutated, cytokinesis phenotypes could be caused by a reduction in importin and/or microtubule binding. However, we previously showed that depolymerizing microtubules using a low dose of nocodazole increases anillin's cortical enrichment, suggesting that reducing anillin's affinity for microtubules should increase anillin's retention or mobility. Because the

($n = 31$) and the C-terminus ($n = 15$) of anillin. The *y*-axis shows the fraction of recovery (corrected) and the *x*-axis shows the time in seconds. The green lines indicate the immobile fraction, while the gray lines show the mobile fraction. The orange lines on the graph indicate the half-life of full-length and C-terminus GFP-tagged anillin. Bars show SD. The table shows the maximum recovery (y_{max}), fluorescence recovery time constant (τ), and half-life ($\tau_{1/2}$) of full-length and C-terminus of anillin. Standard errors are shown in parentheses (SEM).

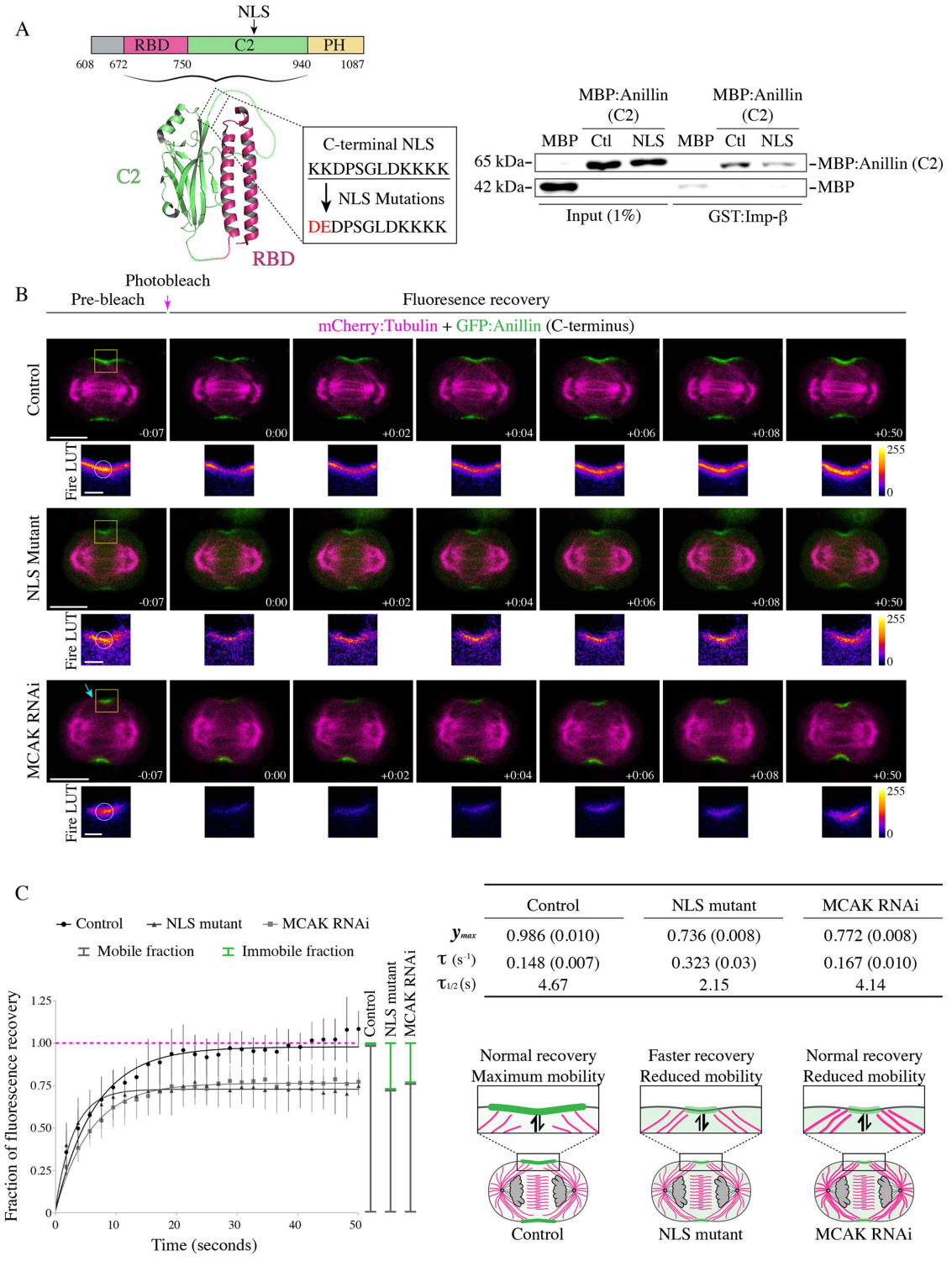

	Control	NLS mutant	MCAK RNAi
y_{max}	0.986 (0.010)	0.736 (0.008)	0.772 (0.008)
τ (s^{-1})	0.148 (0.007)	0.323 (0.03)	0.167 (0.010)
$\tau_{1/2}$ (s)	4.67	2.15	4.14

FIGURE 2: The C-terminal NLS regulates anillin's cortical affinity during cytokinesis. (A) A cartoon schematic shows the C-terminus of anillin with binding domains and the NLS as indicated (magenta = RBD; green = C2; yellow = PH). Underneath is a ribbon structure of the RBD (magenta) and C2 domain (green). The amino acids of the NLS and those that were mutated (850KK851-DE or 887KK888-DE in the longer isoform) are shown in the box. On the right, immunoblots show the in vitro binding of GST-tagged importin-β (Imp-β) with MBP or MBP-tagged C2 domain (Ctl) vs. the C2 domain with the NLS mutations (NLS). Inputs are shown on the left, and pull downs on the right. (B) Time-lapse images show FRAP of HeLa cells expressing mCherry:tubulin (magenta) and GFP-tagged C-terminus of anillin (green), or with the NLS mutations, or after treatment with MCAK RNAi. The boxed insets show the ROIs that were photobleached in Fire LUTs. The scale bars are 10 or 2 μm for boxed insets. The blue arrow points to overextended microtubules. Indicated times are before (–) or after (+) photobleaching. (C) A graph shows the fraction of fluorescence recovery (*y*-axis) over time (*x*-axis; seconds) for control ($n = 15$), NLS mutant anillin ($n = 12$), or after MCAK RNAi ($n = 8$). The green

phenotypes caused by the NLS mutant are the opposite, they more likely arise due to loss of importin binding and a decrease in cortical affinity.

Previous studies showed that the C2 domain can bind to PI4,5P_2 phospholipids (Sun *et al.*, 2015; Budnar *et al.*, 2019). Although the NLS mutations are outside of the putative lipid-binding site, we wanted to be sure that they did not impact lipid binding. We compared the binding profiles of recombinant control GST:anillin RBD + C2 with the NLS mutant using strips blotted with a variety of phospholipids including mono, di-, and triphosphorylated (3,4,5) lipids and found no change in their profiles (Supplemental Figure S2D). Interestingly, there was a strong lipid preference for PI3P. We previously showed that GFP:anillin C-terminus bound preferentially to PI4,5P_2 lipids, suggesting that either the PH domain and/or complexes formed in cells influence anillin's lipid preference (Frenette *et al.*, 2012).

The NLS is autoinhibited by the RBD and is relieved via RhoA binding

Because RhoA is required for anillin's cortical recruitment, we wanted to determine how RhoA binding is coordinated with importin binding. We previously found that the NLS in the C2 domain is intramolecularly inhibited by the RBD, because removing the RBD increases anillin's affinity for importin-β from cell lysates (Beaudet *et al.*, 2017). Here we show that this inhibition is direct because MBP:anillin C2 bound more strongly to GST:importin-β in vitro compared with MBP:anillin C-terminus (Figure 3A and Supplemental Figure S3A). One hypothesis is that active RhoA binding induces a conformational change that makes the C2 more accessible. We tested this model by changing the levels of active RhoA or mutating the RBD and seeing how this influences importin binding. Lysates collected from cells expressing GFP:anillin (C-terminus) were loaded with 5 mM of GDP or GTP to generate higher levels of GTPases bound to GDP or GTP as described previously (Figure 3B and Supplemental Figure S3, B and C; Piekny and Glotzer, 2008). GST:importin-β pulled down more anillin from lysate loaded with GTP compared with lysate loaded with GDP. Because this assay was not selective for RhoA, we determined how altering RhoA activity impacts importin binding. MBP:anillin (RBD + C2) was used to pull down GFP-tagged importin-β from lysates where the C-terminus of Ect2 that contains the GEF domain was overexpressed to increase active RhoA or where Ect2 RNAi was used to deplete endogenous Ect2 to reduce active RhoA (Figure 3C and Supplemental Figure S3D; Solski *et al.*, 2004; Frenette *et al.*, 2012). We found that importin-β was more strongly pulled down with increased levels of active RhoA compared with lysate with reduced levels of active RhoA. We also determined how introducing mutations into the RBD that disrupt RhoA binding (A703E; E721A or A740E; E758A in the longer isoform; Sun *et al.*, 2015) affect anillin's affinity for importin. When MBP:anillin (RBD + C2) containing these RBD mutations was used to pull down GFP-tagged importin-β from lysate, importin binding was drastically reduced compared with control (Figure 3D and Supplemental Figure S3E) regardless of Ect2 levels or activity. These data suggest that importin binding to anillin is regulated by active RhoA, and our model is that RhoA binding causes a conformational change that exposes the NLS in the C2 domain (Figure 3D). It is not clear why GST-tagged importin interacts better with GFP-tagged anillin from cell lysate compared with purified MBP-tagged protein (Figure 3, A and B). One possibility is that the presence and/or binding of other interactors further enhance accessibility of the NLS.

Importin binding enhances anillin's affinity for the cortex

Anillin requires cooperative binding with active RhoA and phospholipids for its recruitment to the equatorial cortex. Because anillin's cortical localization is reduced and delayed when the NLS is mutated, we hypothesize that importin binding stabilizes a conformation that favors one or both of these interactions. To test this, we imaged HeLa cells coexpressing GFP-tagged C-terminus of anillin and H2B:mRuby, and determined how mildly disrupting the interface (I/F) between the RBD and C2 domains (837DFEINIE843 to AFAINIA, or 874DFEINIE880 to AFAINIA in the longer isoform) alone or in combination with the NLS mutant affect anillin's localization (Figure 4, A and B; Piekny and Glotzer, 2008). At anaphase onset, the C-terminus of anillin was broadly cortically localized, followed by its restriction to the equatorial cortex before ingression (Figure 4B). As expected, anillin failed to localize to the cortex when the RBD was mutated (Figure 4B). Mutating the I/F or NLS reduced the breadth of anillin's cortical localization, causing it to be restricted to a narrow region compared with control anillin (Figure 4B). Interestingly, anillin failed to localize to the cortex altogether when the NLS and I/F mutations were combined, similar to the RBD mutant (Figure 4B). We quantified the changes in localization for the different mutants in two ways. First, we measured the breadth of anillin by drawing a line scan around the perimeter of the cell, then added the number of pixels above 50% maximum levels and determined their ratio versus the total number of the perimeter. The ratio of accumulated anillin containing the NLS or I/F mutations was significantly lower compared with control anillin (Figure 4C). Next, we measured the ratio of cortical versus cytosolic anillin, and found that while the I/F mutant was moderately enriched in the cytosol, the I/F + NLS mutant was strongly cytosolic similar to the RBD mutant (Figure 4D). These data suggest that RhoA and importin binding work together to control anillin's cortical localization during cytokinesis.

We further assessed the functional requirement for these mutations during cytokinesis. Constructs containing RNAi-resistant GFP-tagged full-length anillin, or with mutations in the NLS, I/F, or both, were expressed in HeLa cells depleted of endogenous anillin and coexpressing mCherry:tubulin to visualize the mitotic spindle. Cells were imaged after anaphase onset to assess localization and cytokinesis phenotypes (Figure 5A). In control cells, anillin was first visible at the cortex 2 min after anaphase onset and by 6 min had accumulated at the equatorial cortex where it remained associated with the furrow through ingression (Figure 5A). As expected, 100% of the cells successfully ingressed (Figure 5A). Cortical recruitment of the I/F mutant was delayed until 4 min after anaphase onset, and restricted to a narrow region. A small proportion of cells expressing the I/F mutant failed cytokinesis (22.7%; Figure 5A), and those that completed ingression took longer compared with control cells (17.8 ± 4.3 min vs. 12.3 ± 2.7 min; Figure 5B). As previously reported,

lines indicate the immobile fraction, while the gray lines show the mobile fraction. Bars show SD. The table shows the maximum recovery (y_{max}), fluorescence recovery time constant (τ), and half-life ($\tau_{1/2}$) for each condition as indicated. SEM are shown in parentheses. Below the table, cartoon schematics of cells show how mutating the NLS causes a faster recovery vs. MCAK RNAi, which recovers similar to control. However, both the NLS mutant and MCAK RNAi have reduced mobility.

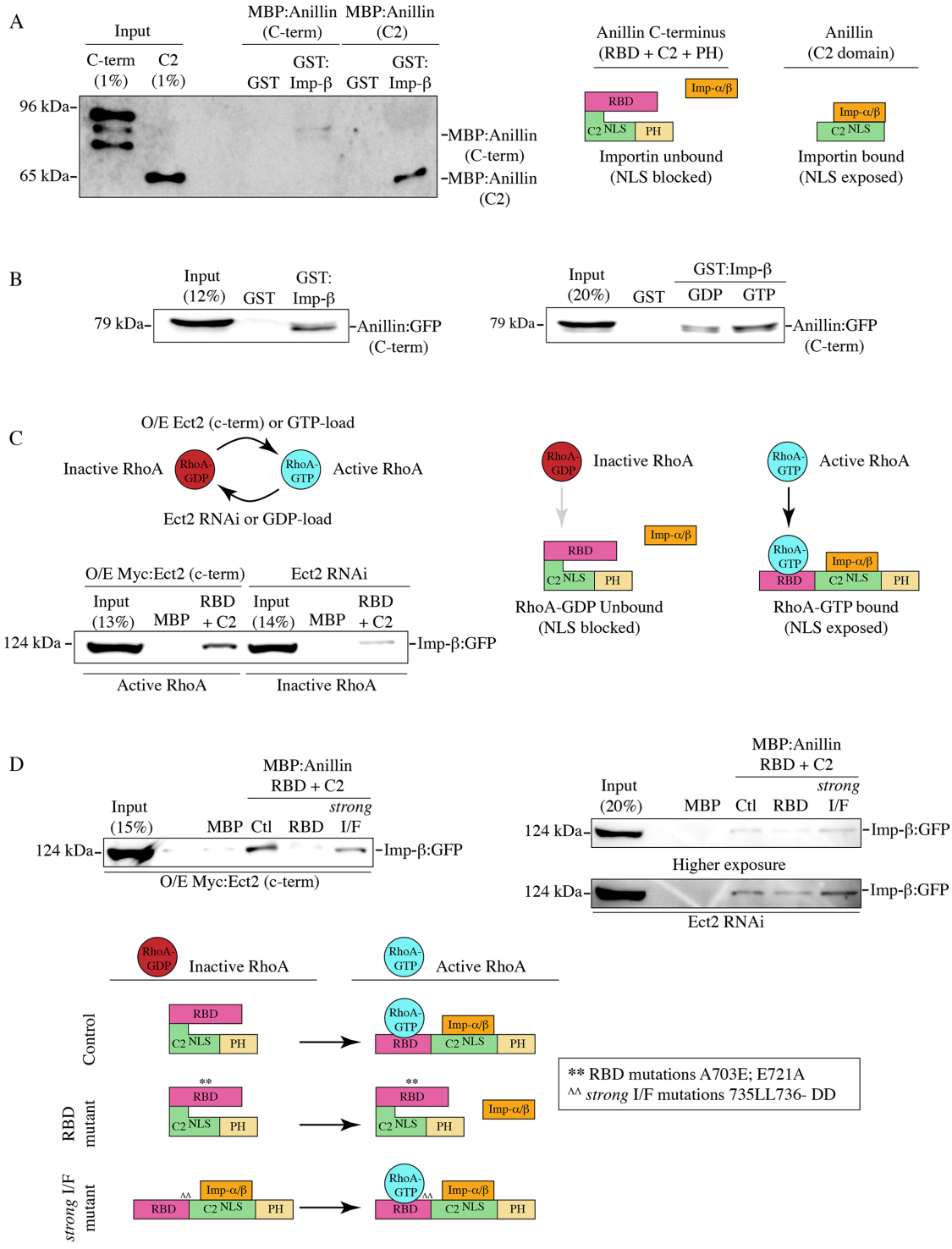

FIGURE 3: The NLS is inhibited by the RBD and is relieved by RhoA binding. (A) Immunoblots show in vitro binding of purified GST or GST-tagged importin-β (Imp-β) with MBP-tagged C-terminus of anillin (C-term; top) or the C2 domain (bottom). A cartoon schematic shows how the C-terminal NLS within the C2 domain (green) is exposed for importin binding (orange) in the absence of the RBD domain (magenta; PH domain in yellow). (B) Immunoblots show pull downs of GFP-tagged C-terminus of anillin (C-term) from HeLa cell lysates with purified GST or GST-tagged importin-β (left). Cell lysates were preloaded with 5 mM GDP or 5 mM GTP as indicated (right). (C) An immunoblot shows pull downs of GFP-tagged importin-β from lysates from cells overexpressing (O/E) Myc-tagged Ect2 C-terminus to generate active RhoA (left), or after Ect2 RNAi to reduce active RhoA (right), with purified MBP or MBP-tagged anillin (RBD + C2). Cartoon schematics show how active RhoA (RhoA-GTP) or inactive RhoA (RhoA-GDP) impact anillin's affinity for importins. (D) Immunoblots show pull downs of GFP-tagged importin-β from lysates as in C with MBP, MBP-tagged anillin (RBD + C2; Ctl) or with RBD mutations that disrupt RhoA binding (A703E; E721A or A740E; E758A in the longer isoform; RBD), or mutations that strongly disrupt the RBD-C2 interface (735LL736-DD or 772LL773-DD in the longer

cortical recruitment of the NLS mutant was also delayed and restricted to a narrow region. A subset of these cells failed cytokinesis (36.4%; Figure 5A), and those that completed ingression took longer compared with control cells (16.4 ± 3.5 mins; Figure 5B; Beaudet *et al.*, 2017). Anillin containing both the NLS and the I/F mutations failed to localize to the cortex, and the majority of cells failed cytokinesis (70.6%; Figure 5A). Cells that ingressed successfully were significantly delayed compared with control cells (19.2 ± 1.6 mins; Figure 5B).

To further assess how these mutations affect cytokinesis at the population level, we performed experiments as above on asynchronous populations of HeLa cells. We calculated the proportion of binucleate cells for each construct as a readout for cytokinesis failure (Figure 5C). There was a significant increase in the proportion of binucleate cells depleted of endogenous anillin and expressing RNAi-resistant I/F mutant anillin (49.5% compared with cells expressing control anillin 23.5%), which was also observed in cells expressing the NLS mutant (47.7%). However, there was an even greater increase in the proportion of binucleate cells expressing anillin with both the NLS and the I/F mutations, which was similar to the anillin RNAi control (68.7% vs. 72.3%, respectively). These data show that weakening the interface of the RBD and C2 causes a dramatic change in anillin's recruitment when importin binding is lost, suggesting that there is feedback from the C2 domain to the RBD to facilitate phospholipid and/or RhoA binding (Figure 5D).

Cortical recruitment of anillin relies on the interface between the RBD and C2

Our data shows that the relative positions of the RBD and C2 domains are crucial for anillin function. To further test how the interface mediates anillin's ability to interact with importin-β or RhoA, we created point mutations within the RBD to specifically disrupt hydrophobic interactions between the RBD and C2 domain (735LL736 -DD or 772LL773-DD in the longer isoform; *strong* I/F mutant; Figure 6A). Based on their position, these mutations should reduce binding between the αB helix and the C2 domain to more strongly disrupt the interface compared with the I/F mutations described earlier. Importantly, the *strong* I/F mutations should not interfere with RhoA binding, which occurs through a different interface on the αA and αB helices (Supplemental Figure S4A; Sun *et al.*, 2015). First, we assessed how the *strong* I/F mutations affect autoinhibition of the NLS in the C2 domain. We previously showed that the C-terminus of anillin fails to localize to the nucleus in interphase cells, but is nuclear after removing the RBD (Beaudet *et al.*, 2017). We measured changes in the nuclear localization of the C-terminus of GFP-tagged anillin with mutations in the NLS, *strong* I/F, or *strong* I/F + NLS. Based on relative levels, their distribution was categorized as nuclear or cytosolic, and only considered if their average fluorescence intensity was more than 1200 a.u. Nuclear localization was determined by the ratio of the average fluorescence intensity of anillin in the nucleus over the average intensity of anillin in the cytosol, where $R > 1.25$ was "nuclear" and $R < 1.25$ was "cytosolic" (Supplemental Figure S4B). As expected, the C-terminus localized primarily to the cytosol in interphase cells (Figure 6B). Introducing the *strong* I/F mutations caused the C-terminus to localize to the nucleus in 64% of the cells, which was lost when the NLS was also mutated (Figure 6B). Therefore, the *strong* I/F mutations partially relieve autoinhibition from the RBD.

Next, we determined how the *strong* I/F mutant affects importin binding after manipulating active RhoA or RhoA binding as described in Figure 3C. We used recombinant MBP:anillin (RBD + C2) control, RBD mutant, or the *strong* I/F mutant to pull down GFP-tagged importin-β from lysates +/– active RhoA (Figure 3D). Active RhoA was generated by overexpression (O/E) of the C-terminus of Ect2 (Myc:Ect2 [C-term]), and Ect2 RNAi was used to reduce active RhoA. We found that importin-β had similar affinity for the *strong* I/F mutant compared with control anillin in the presence of active RhoA and higher affinity in the absence of active RhoA, while the RBD mutant showed lower affinity in either case (Figure 3D). These data suggest that the *strong* I/F mutant mimics an "open" conformation that no longer requires RhoA binding for increased accessibility of the NLS and other binding sites, and binds to importin with stronger affinity compared with nonmutant anillin (Figure 3D).

Next, we determined how disrupting the interface affects anillin's localization and function during cytokinesis. HeLa cells coexpressing GFP-tagged C-terminus of anillin or the *strong* I/F mutant and H2B:mRuby to visualize chromatin, were imaged after anaphase onset. As previously described, anillin localized to the cortex ~2 min after anaphase onset and accumulated at the equatorial cortex during ingression. However, anillin containing the *strong* I/F mutations failed to localize to the cortex and remained cytosolic through ingression (Figure 6C). To determine how the *strong* I/F mutant impacts anillin's function for cytokinesis, RNAi-resistant GFP-tagged full-length anillin or containing the *strong* I/F mutations were imaged in HeLa cells depleted of endogenous anillin and coexpressing mCherry:tubulin (Figure 6D). Full-length anillin localized similar to the C-terminus as previously described and all cells completed ingression, while the *strong* I/F mutant failed to localize to the cortex and the majority of cells failed to ingress (62.5%; Figure 5B). Cells that successfully ingressed were significantly delayed compared with control cells (18.3 ± 2.4 min; Figure 5B). Thus, the localization and phenotype of the *strong* I/F mutant resembles constructs containing mutations in the RBD that disrupt RhoA binding, or in the C2 domain that weakly disrupt the I/F (837DFEINIE843 to AFAINIA) and the NLS. However, we do not think that the I/F mutations disrupt RhoA binding per se, because MBP:anillin (RBD + C2) containing the *weak* or *strong* I/F mutations pulled down GFP:RhoA from lysates (Supplemental Figure S4C). In addition, we previously reported that the *weak* I/F mutations bind to RhoA, albeit ~1.5- to 2-fold weaker compared with control (Piekny and Glotzer, 2008). We also tested the lipid preference of the *strong* I/F mutant as described earlier and found that there was no significant difference in the lipid binding profile compared with control anillin (Supplemental Figure S2D). Lastly, we assessed how the *strong* I/F mutations impact cytokinesis at the population level and found that the proportion of binucleate cells was similar to the anillin RNAi control (71.0% vs. 72.3%; Figure 5C). These data suggest that the cortical affinity of anillin is regulated by importin binding, which feeds back through the interface to

isoform; *strong* I/F). Underneath, cartoon schematics show how RhoA-GTP (blue) binding to the RBD (magenta) relieves inhibition of the C2 domain (green; NLS is indicated) to enable importin-α/β (orange) binding to the NLS (PH domain is in yellow). Mutating the RhoA-binding domain (RBD mutant) to block RhoA binding causes failure of the C-terminus to undergo conformational changes required for importin binding. Mutations that strongly perturb the intramolecular interface (*strong* I/F mutant) remove autoinhibition of the RBD, causing importin to bind more strongly to anillin regardless of RhoA binding.

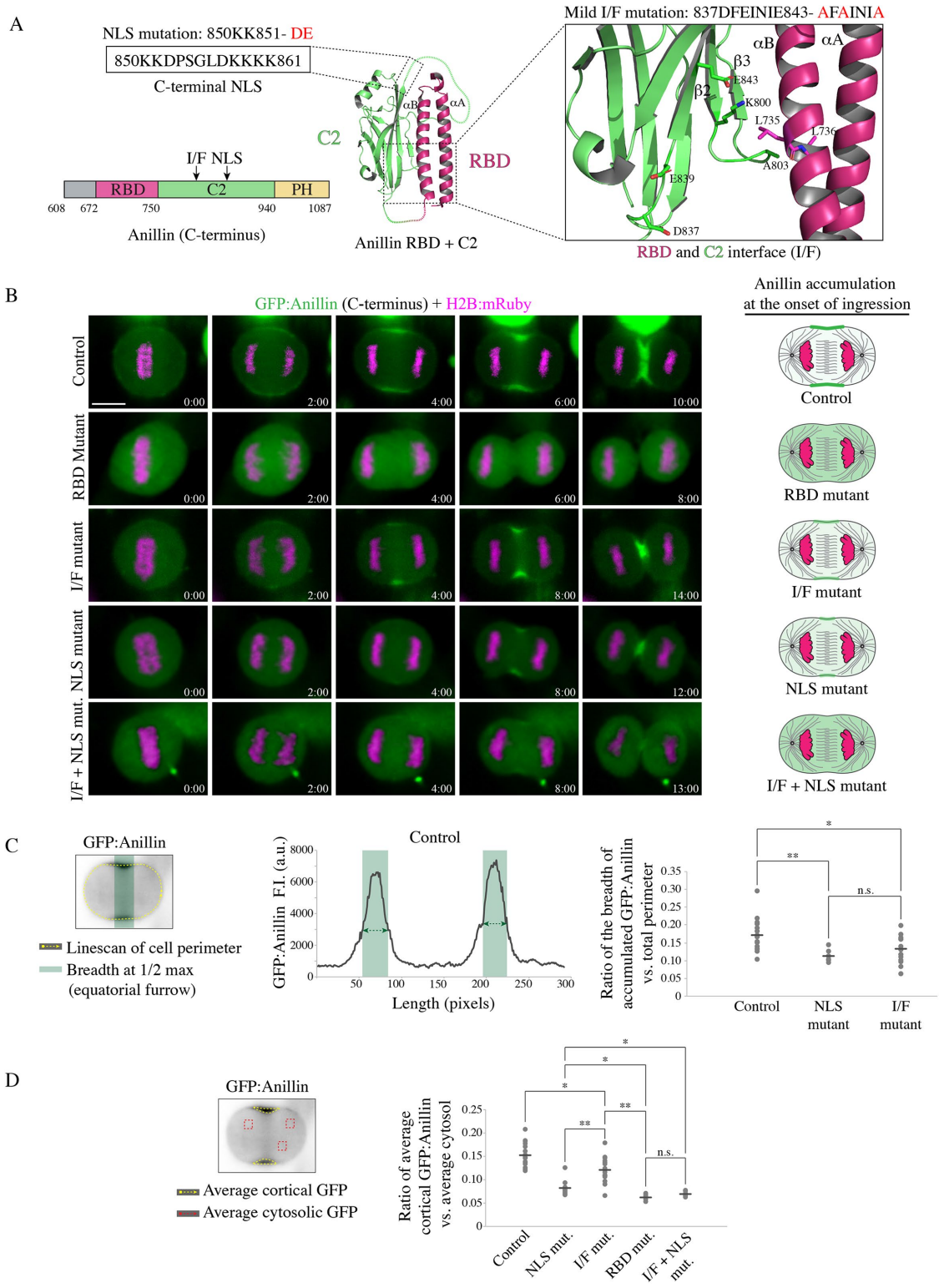

FIGURE 4: Importin binding enhances anillin's affinity for the equatorial cortex. (A) A ribbon structure shows the intramolecular interface between the RBD (magenta) and the C2 domain (green). The boxed inset (right) shows the amino acids that form electrostatic and hydrophobic interactions at the interface. The amino acids that were mutated to generate mild perturbations of the interface (I/F mutant) are positioned in the C2 domain (I/F mutant; 837DFEINIE843-AFAINIA or 874DFEINIE880-AFAINIA in the longer isoform). These mutations are predicted to disrupt electrostatic interactions (E843-K800 or E880-K837 in the longer isoform) with the disordered loop between the β2 and β3 strands in the C2 domain, which interfaces the RBD. The mutated amino acids in the NLS (850KK851-DE or 887KK888-DE in the longer isoform) are shown in the boxed inset to the left. (B) Time-lapse images show HeLa cells expressing different GFP-tagged C-terminus anillin constructs (green) and H2B:mRuby (magenta; to show chromatin) as indicated: control ($n = 18$), RBD mutant that disrupts RhoA binding (A703E; E721A or A740E; E758A in the longer isoform; $n = 5$), RBD-C2

influence anillin's cortical recruitment. Binding too weakly, or too strongly, to importin prevents cooperative binding to phospholipids and active RhoA for cortical localization and function.

DISCUSSION

Our studies shed light on how anillin's function for cytokinesis is regulated at the intramolecular level by active RhoA and importin-β. Our previous study showed that cytokinesis is regulated by Ran-GTP, which may coordinate ring positioning with chromatin (Beaudet *et al*., 2017). We also showed that anillin is a target of this pathway, as it contains a highly conserved NLS that binds to importin-β and is required for its proper localization and function during cytokinesis (Beaudet *et al*., 2017). As described earlier, a gradient of active Ran persists around chromatin, and importin-bound cargoes form an inverse gradient (Kaláb and Heald, 2008). Having high levels of importins free to bind to cargo near the equatorial cortex could help regulate cortical proteins required for cytokinesis. Here we delve into the mechanism by which importin binding regulates anillin function. Our model is that when the levels of active RhoA increase upon anaphase onset, the binding of active RhoA to the RBD causes a conformational change in anillin that makes the neighboring C2 domain more accessible to binding partners. One of these partners is importin-β, which binds to the NLS in the C2 domain and may stabilize a conformation that favors binding to active RhoA. Importin-β subsequently could be outcompeted by phospholipids to mediate cooperative binding for anillin's recruitment and retention at the equatorial cortex (Figure 6E). Our FRAP data supports this model by showing that the NLS, which binds to importins, influences properties of the C-terminus of anillin that promote its enrichment at the equatorial cortex (Figures 1 and 2). Further, our binding data shows that active RhoA increases anillin's affinity for importin (Figure 3). Our localization data also shows the importance of the interface between the RBD and C2 domain, which is required for cortical recruitment (Figures 4–6). Weakening this interface makes importin binding crucial, because it helps stabilize anillin's conformation for RhoA binding (Figures 4 and 5). More strongly disrupting the interface causes importin-β to bind more strongly and prevents cortical recruitment altogether, which is reminiscent of findings from our previous study showing that the overexpression of importin-β reduces anillin's cortical localization (Figures 3D and 6; Beaudet *et al*., 2017).

Importin binding regulates anillin's affinity for the equatorial cortex

Anillin is recruited to the equatorial cortex by active RhoA, and is restricted from the polar cortices by astral microtubules. Previous studies showed that reducing active RhoA or stabilizing microtubules with Taxol increase anillin's localization to microtubules, suggesting that they compete with each other (van Oostende Triplet *et al*., 2014). We also found that mutating the NLS to reduce importin binding weakens anillin's cortical affinity because its recruitment is delayed and more restricted compared with nonmutant anillin. In addition, disrupting astral microtubules causes the NLS mutant to spread along the cortex, suggesting that the weakened affinity favors a transition in its localization to microtubules (Beaudet *et al*., 2017). Here we continued to explore how importin binding affects anillin's cortical exchange by performing FRAP studies. NLS mutations that reduce importin binding decreased anillin's mobility and increased its rate of recovery (Figure 2). However, it is important to note that the NLS mutations could impact other binding partners that could also contribute to the observed results. For instance, the reduced mobility likely reflects the shift onto microtubules, because we also saw reduced mobility of anillin when microtubules were overextended by MCAK RNAi (Figure 2). Interestingly, when the NLS is mutated, anillin's affinity for microtubules is not increased per se, because we found via cosedimentation assays that its affinity is partially reduced (Supplemental Figure S2B). Thus, the reduced mobility seen in the NLS mutant may be indirect and due to an increase in microtubule localization caused by an overall reduced affinity for RhoA. We also saw increased recovery with the NLS mutant that we did not see with MCAK RNAi, which may indicate that importin binding specifically regulates cortical retention.

RhoA binding relieves autoinhibition of the C2 domain from the RBD

We previously found that the C2 domain in the C-terminus of anillin had a higher affinity for importin and microtubules when the RBD was removed (Beaudet *et al*., 2017). Because the RBD binds to active RhoA, we proposed a model where active RhoA binding could induce a conformational change that makes the C2 more accessible. Here, we tested this model by changing the levels of active RhoA, or mutating the RBD and seeing how this influenced importin binding. In support of our model, when active RhoA levels were high (e.g., overexpressed GEF domain of Ect2), we saw increased importin binding compared with when active RhoA levels were low (e.g., Ect2 RNAi), or when the RBD was mutated (Figure 3). Thus, similar to other RhoA effectors, such as mDia, intramolecular autoinhibition could ensure that anillin's other interactions, such as binding to phospholipids, are closely linked to when active RhoA levels increase during mitotic exit and in the region of the equatorial cortex (Li and Higgs, 2003; Lammers *et al*., 2005).

Feedback at the interface between the RBD and C2 domain drives anillin's equatorial recruitment

Our data shows that the NLS of anillin influences its cortical exchange dynamics. One hypothesis is that the C2 domain feeds back to the RBD to increase RhoA binding, either by improving accessibility

interface mutant (I/F mutant; 837DFEINIE843-AFAINIA; $n = 15$), NLS mutant (850KK851-DE; $n = 12$), and a combination of the I/F + NLS mutations ($n = 8$). Times are indicated from anaphase onset. The scale bar is 10 μm. Cartoon cells to the right show changes in the distribution of anillin (magenta) at the onset of ingression for the different constructs as indicated. (C) The graph shows an example of a line scan for the control construct in B, with fluorescence intensity on the *y*-axis and length (pixels) on the *x*-axis. The line scan (dotted yellow) was drawn as shown on the cell image (upper left). Regions of the cortex above 50% maximum levels are highlighted in green and represent accumulated anillin. To the right, a dot plot shows changes in the ratio of the breadth of accumulated anillin vs. total cell perimeter (*y*-axis) for the control and mutants as indicated. The means are indicated by the dark-gray lines, and significance was determined using the unpaired Student's *t* test (n.s., not significant; *, $p < 0.05$; **, $p < 0.001$). (D) The cell image (left) shows the area (yellow dotted line) measured to determine the average intensity of GFP-tagged anillin at the cortex, and the ROIs (red boxes) used to calculate the average intensity of anillin in the cytosol. The dot plot shows the average ratio of cortical anillin vs. cytosol (*y*-axis) for the control and mutants in B as indicated. The means are indicated by the dark-gray lines, and significance was determined using the unpaired Student's *t* test (n.s., not significant; *, $p < 0.05$; **, $p < 0.001$).

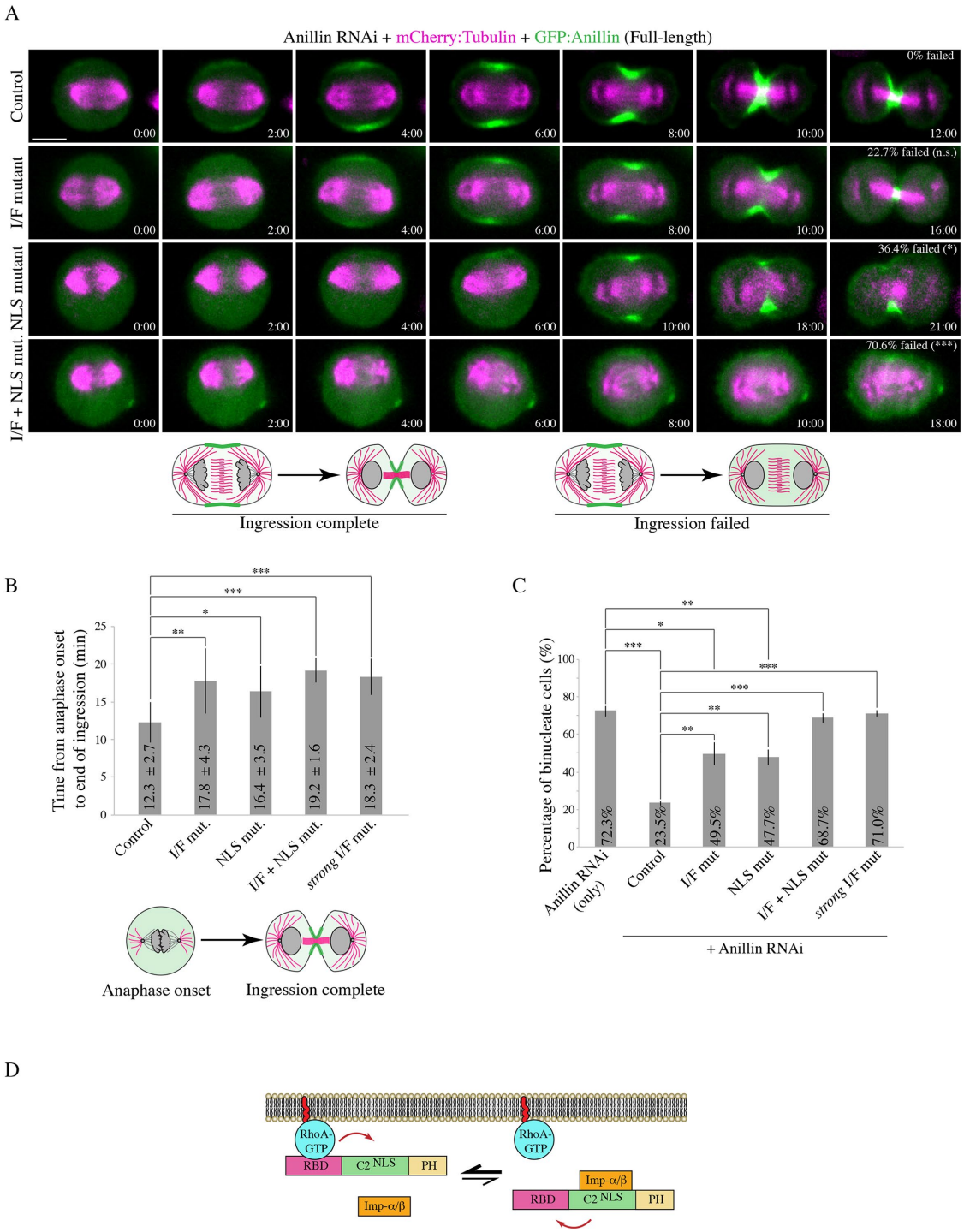

FIGURE 5: Anillin requires importin binding and the interface between the RBD and C2 domain for cytokinesis. (A) Time-lapse images show HeLa cells treated with anillin RNAi to deplete endogenous anillin, expressing various RNAi-resistant GFP-tagged full-length anillin constructs (green) and mCherry:tubulin (magenta) as indicated: control (n = 15), RBD-C2 mild interface mutant (I/F mutant; n = 22), NLS mutant (n = 22), and a combination of the mild I/F + NLS mutations (I/F + NLS mut.; n = 17). Times are indicated from anaphase onset. The scale bar is 10 μm. For each condition, the percentage of cells that failed ingression are shown. The data were analyzed using two-tailed Fisher's exact test (n.s., not significant; *, $p < 0.05$; ***, $p \leq 0.0001$). Below are cartoon schematics illustrating a cell that has completed ingression vs. a cell that failed ingression. (B) A bar graph shows the time from anaphase onset to the end of ingression (*y*-axis) in cells rescued with the various anillin constructs in A: control (n = 15), I/F mutant (n = 17), NLS mutant (n = 14), I/F + NLS mutant (n = 5), and *strong* I/F mutant (n = 6). Bars indicate SD. Data was analyzed and p values were determined by unpaired Student's *t* test (*, $p < 0.05$; **, $p < 0.001$; ***, $p \leq 0.0001$). The cartoon cells below illustrate how time from anaphase onset to the end of ingression was defined. (C) A bar graph shows the percentage of binucleate cells (*y*-axis) as a readout for cytokinesis failure in populations of asynchronous HeLa cells after anillin RNAi and coexpressing with the indicated RNAi-resistant constructs. Bars show SD (n = 3 replicates with 60–180 cells counted

to active RhoA or by reducing its dissociation. Indeed, when the NLS mutations were combined with mutations that weaken the interface between the RBD and C2, anillin failed to be recruited to the cortex and failed to support cytokinesis, similar to mutations that disrupt the RBD (Figures 4 and 5). Introducing mutations predicted to more strongly disrupt the interface similarly failed to localize or function (Figure 6). However, in this case, anillin bound more strongly to importin, which may outcompete interactions with phospholipids for cooperative binding. Thus, we propose that feedback between the RBD and C2 domains is crucial for optimal binding to both RhoA and importin. Because the C2 domain has binding sites for other factors, it would be interesting to determine how these other interactions also impact binding to RhoA and vice versa. For example, as described above, stabilizing microtubules competes anillin from the cortex. Because the microtubule- and importin-binding sites overlap, stabilizing microtubules may outcompete importins and sterically hinder the RBD for optimal RhoA binding. In addition, previous studies suggest that there is cooperativity between anillin's interaction with phospholipids and RhoA, which could involve a feedback mechanism (Sun *et al.*, 2015; Budnar *et al.*, 2019). The lipid-binding site is predicted to be at a loop near the NLS, and lipid binding could increase accessibility of the RBD to RhoA, similar to importin. Anillin likely is also regulated by posttranslational modifications that may influence its conformation. For example, a recent study showed that phosphorylation at a site that lies just N-terminal to the RBD enhances anillin's cortical association and is required for cytokinesis (Kim *et al.*, 2017). This area is underexplored and it would be interesting to see how phosphorylation by different cell cycle kinases influences anillin's structural changes and function for cytokinesis.

MATERIALS AND METHODS

Cell culture

HeLa cells were plated and grown in DMEM (Wisent), supplemented with 10% fetal bovine serum (Thermo Scientific), 2 mM L-glutamine (Wisent), 100 U penicillin, and 0.1 mg/ml streptomycin (Wisent), and were maintained at 37°C with 5% CO_2. For transfection, cells were plated in DMEM media without antibiotics (PS), and transfected using Lipofectamine 2000 according to the manufacturer's protocol (Invitrogen), except that 3 µl of Lipofectamine was used per 2 ml of media with 0.5–2.0 µg DNA and 3 µl of 2 nM siRNAs, as described previously (Yüce *et al.*, 2005; Piekny and Glotzer, 2008). Cells were imaged 24–26 h after DNA transfection, and 27–30 h after cotransfection of DNA and siRNAs. Anillin and Ect2 were used as described previously (Yüce *et al.*, 2005; Piekny and Glotzer, 2008; van Oostende Triplet *et al.*, 2014).

Plasmids

H2B:mRuby was generated from H2B:GFP, generously provided by G. Hickson (University of Montreal). GFP was replaced with mRuby using *Bam*HI (New England Biolabs) and *Xba*I restriction enzymes (New England Biolabs), and the pcDNA3:mRuby2 plasmid was kindly provided by C. Brett (Concordia University). A stable HeLa mCherry:tubulin cell line was generated previously (van Oostende Triplet *et al.*, 2014). pEGFP-N1:importin-β was obtained by Addgene, made by P. Lavia (plasmid #106941). GST:importin-β was made by cloning importin-β cDNA from the pEGFP-N1 vector into pGEX-4T using *Nco*I and *Not*I (New England Biolabs). The anillin constructs for mammalian cell expression (GFP-tagged) or protein expression (MBP or GST-tagged) were generated previously (Piekny and Glotzer, 2008; Frenette *et al.*, 2012). The 850KK851-DE or 887KK888-DE (NLS mutant), A703E; E721A or A740E; E758A (RBD mutant; Sun *et al.*, 2015), 837DFEINIE843-AFAINIA or 874DFEINIE880-AFAINIA (*weak* I/F mutant; Piekny and Glotzer, 2008), 735LL736-DD or 772LL773-DD (*strong* I/F mutant) and combinations of mutations were generated in the anillin constructs by quikchange PCR. The His:RhoA and Myc:Ect2 (C-terminus) constructs were generated previously (Yüce *et al.*, 2005; Frenette *et al.*, 2012). All constructs were verified by sequencing.

Microscopy

Cells were fixed for immunofluorescence using 10% trichloroacetic acid as described previously (Yüce *et al.*, 2005). Fixed cells were immunostained for microtubules using 1:250 mouse anti-tubulin antibodies (DM1A; Sigma-Aldrich), anillin using 1:200 rabbit polyclonal anti-anillin antibodies (Piekny and Glotzer, 2008), and GFP using 1:100 mouse clones 7.1 and 13.1 (Roche) or 1:200 rabbit anti-GFP polyclonal antibodies generously provided by M. Glotzer (University of Chicago). Anti-rabbit or -mouse Alexa 488 and anti-mouse or -rabbit Alexa 568 (Invitrogen) secondary antibodies were used at a 1:250 dilution. DAPI (Sigma-Aldrich) was added at a 1:1000 dilution (1 mg/ml stock) for 5 min before mounting the coverslips onto slides. Fixed cells were imaged using a Leica DMI6000B wide-field microscope with the 63×/1.4 PL APO oil immersion objective (pixel size 0.102 µm), and Z-stacks of 0.5 µm were acquired with a Hamamatsu OrcaR2 camera and Volocity software (PerkinElmer) using a piezo Z stage (MadCityLabs). Image files were exported as TIFFs, which were opened with ImageJ (National Institutes of Health; NIH) and converted into maximum intensity Z-stack projections. Projections and merged color images were then converted into 8-bit images and imported into Illustrator (Adobe) to make figures.

To perform live imaging, media was replaced with phenol red–free DMEM media. Cells were plated and transfected on 25-mm round coverslips (no. 1.5) placed in a 35-mm Chamlide magnetic chamber (Quorum). Cells were kept at 37°C with 5% CO_2 using the INU-TiZ-F1 chamber (MadCityLabs). Live imaging was performed on an inverted Nikon Eclipse Ti microscope with a Livescan Swept Field confocal unit (Nikon), using the 60×/1.4 CFI PLAN APO VC oil immersion objective (pixel size 0.27 µm), a piezo Z stage (MadCityLabs), and with the iXON897 EMCCD camera (Andor). Images were acquired with 200 ms exposures using the 488- and 561-nm lasers (100 mW; Agilent) set between 20 and 40% power, depending on the intensity of fluorescent signals (settings were kept constant for related experiments), and multiple Z-stacks of 0.5 µm were taken every 60 s per cell using NIS-Elements acquisition software (Nikon), and a narrow GFP or dual filter (500–544 and 600–665 nm; Chroma). All of the images coexpressing GFP and mRuby probes were spectrally unmixed using the NIS-Elements acquisition software (Nikon). Image files were exported as TIFFs, which were opened with ImageJ (NIH) and converted into maximum intensity Z-stack projections. Projections and merged color images were then converted into 8-bit images and imported into Illustrator (Adobe) to make figures.

per replicate for each condition). Data was analyzed and *p* values were determined by the unpaired Student's *t* test (**, $p < 0.001$; ***, $p \leq 0.0001$; n.s., not significant- not shown). (D) A schematic shows how importin binding (orange) may increase RhoA binding (RhoA-GTP in blue; RBD in magenta) or reduce its cortical dissociation by stabilizing a favorable conformation of the RBD and C2 domain (green; NLS also shown). The PH domain is in yellow.

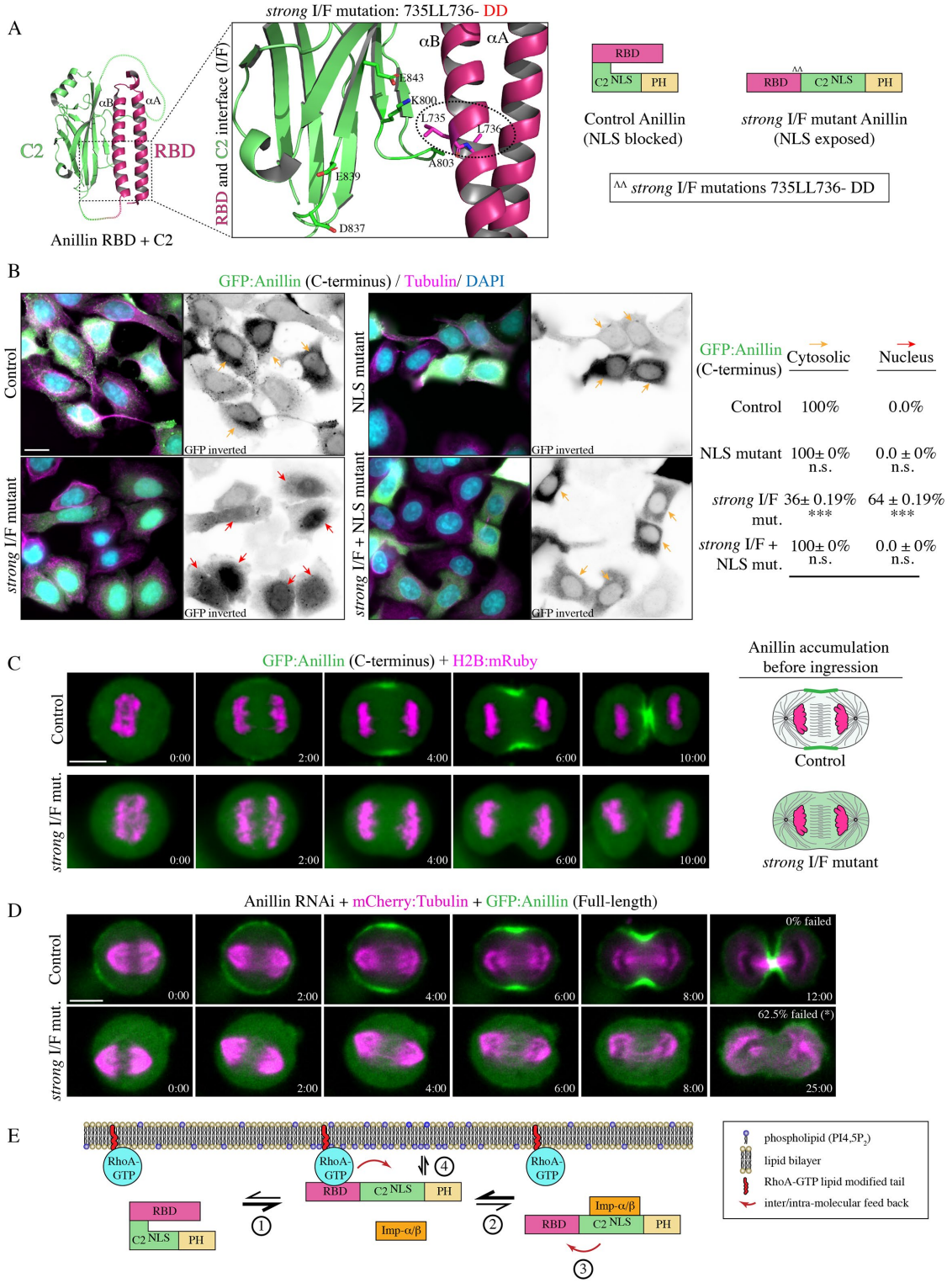

FIGURE 6: Disrupting the interface strengthens importin binding and blocks cytokinesis. (A) A ribbon structure shows the intramolecular interface between the RBD (magenta) and the C2 domain (green). The boxed inset shows the amino acids that form electrostatic and hydrophobic interactions at the interface. The amino acids that were mutated to generate a *strong* I/F mutant are positioned in the αB helix and are circled (L735D; L736D, or L772D; L773D in the longer isoform). The amino acids that mediate RhoA binding map to the αA and αB helices, and are positioned away from the C2 domain (Supplemental Figure S4B). To the right is a cartoon schematic illustrating how *strong* I/F mutations are predicted to disrupt the structure of anillin. (B) Images show fixed HeLa cells expressing GFP-tagged anillin C-terminus, or the NLS mutant, *strong* I/F mutant, or *strong* I/F + NLS mutant, stained for GFP (green), tubulin (magenta), and DAPI (DNA; blue). Yellow arrows point to cytosol localization, while red arrows point to nuclear localization. To the right, the percentage of cytosolic vs. nuclear localization is indicated for each condition. SD are

FRAP

To perform FRAP experiments, cells were plated and transfected on 25-mm round coverslips (no. 1.5) placed in a 35-mm Chamlide magnetic chamber (Quorum). Cells were kept at 37°C with 5% CO_2 using the INU-TiZ-F1 chamber (MadCityLabs). Live imaging and FRAP were performed using a Nikon C2 laser scanning confocal microscope using the 100× Plan Apo I (NA1.4) objective and Elements 4.0 acquisition software (Nikon). Time-lapse images were acquired at a resolution of 1024 × 1024 pixels every 2 s for a total of 60 s. Two time points were acquired before photobleaching and for up to 50 s after photobleaching. Photobleaching of control and experimental ROI's took place for a total of 5 s by pulsing 10 times with the laser power set between 20 and 50%. Movies were exported as TIFFs, then opened with ImageJ (NIH) for analysis. The fluorescence intensities of bleached and nonbleached ROIs were corrected for acquisition bleaching and normalized to background. The average intensity of each ROI was plotted over time using Prism software, and the signal recovery rate and maximum recovery of signal was determined using nonlinear regression fitting with the following formula:

$$F(t) = y_{max}(1 - e^{-\tau t})$$

where $F(t)$ describes the fraction of fluorescence recovery for each time point after photobleaching compared with the prebleached signal, y_{max} describes the maximum FRAP, and τ describes the time constant for fluorescence signal recovery. The half-life ($\tau_{1/2}$) or time taken to reach half the maximum FRAP was determined by the following equation:

$$\tau_{1/2} = \ln(2)/\tau$$

and the immobile fraction was determined as follows:

$$F_{imm.} = 1 - y_{max}$$

where $F_{imm.}$ is the percent difference between the initial average fluorescence signal before photobleaching and the maximum signal recovered (y_{max}) after photobleaching.

Protein purification, pull downs, and protein-lipid overlay assays

The following proteins were made from *Escherichia coli* BL21 cells: His:RhoA, GST, GST:importin-β, GST:anillin (AHD; 608–940), MBP, MBP:anillin (C2; 750–872), MBP:anillin (RBD + C2; 672–872), and MBP:anillin (C-term; 608–1087), as well as containing mutations described earlier. Bacteria were resuspended in lysis buffer (2.5 mM $MgCl_2$, 50 mM Tris, 150 mM NaCl, pH 7.5, 0.5% Triton X-100, 1 mM dithiothreitol [DTT], 1 mM phenylmethanesulfonyl fluoride [PMSF], and 1× protease inhibitors [Roche]), incubated with 1 mg/ml lysozyme on ice for 30 min, then sonicated three times. Extracts were incubated with preequilibrated amylose resin (New England Biolabs) or glutathione sepharose 4B (GE Lifesciences) for 5 h or overnight at 4°C with rotation. After washing, beads were stored as a 50% slurry at 4°C or eluted in equivalent volumes of 100 mM maltose or 10 mM glutathione (pH 8.0) on ice for 2 h. Protein concentration was determined by running samples by SDS–PAGE and measuring the density of bands in comparison to known concentrations of bovine serum albumin and/or by Bradford assay for eluted proteins.

To test for binding, proteins were pulled down from cell lysates after transfection or using eluted recombinant purified protein. Transfected HeLa cells were lysed in 50 mM Tris, pH 7.6, 150 mM NaCl, 5 mM $MgCl_2$, 0.5% Triton X-100, 1 mM DTT, 1 mM PMSF with 1× protease inhibitors (Roche), and incubated with 5–10 µg of purified MBP-tagged anillin or GST-tagged importin-β protein on beads at 4°C overnight. Eluted proteins were added to beads at final concentrations as indicated. After binding, beads were washed three to four times with 50 mM Tris, pH 7.6, 150 mM NaCl, 5 mM $MgCl_2$ before adding SDS sample buffer to denature the proteins for SDS–PAGE. All samples were run by SDS–PAGE and wet-transferred to nitrocellulose membrane for Western blotting. All blots were reversibly stained with Ponceau S to show total protein. The blots were blocked with 5% milk for 20 min, then incubated with either mouse anti-MBP antibodies at a dilution of 1:5000 (New England Biolabs) or 1:2500 mouse anti-GFP antibodies (Roche) in 1× PBS-T (0.140 M NaCl, 2.7 mM KCl, 10 mM Na_2HPO_4, 1.8 mM KH_2PO_4, 0.5% Triton X-100) for 1–2 h at room temperature. After washing the membrane three to four times with 1× PBS-T, secondary antibodies (anti-rabbit HRP [horseradish peroxidase] or anti-mouse HRP; Cedarlane) were added as per manufacturer's instructions in 1× PBS-T for 1 h. The blots were developed using enhanced chemiluminescence (ECL) Western blotting detection reagents (GE Amersham) and visualized on a GE Amersham Imager 600. All results from each pull-down assay were replicated in at least three distinct experiments to ensure reproducibility.

PIP strip membranes that have been spotted with various phosphoinositides and other biological relevant lipids (Echelon Biosciences) were blocked with 3% skim milk in 1× TBS-T at 4°C overnight. PIP strips were removed from blocking solution and incubated with 1 µg/ml purified recombinant anillin constructs for 2 h at room temperature. After washing three to four times with 1× TBS-T, the strips were incubated with 1:10,000 mouse anti-GST antibodies (Sigma). The secondary antibody (anti-mouse HRP) was then added in 1× TBS-T for 1 h. After washing the membranes three to four times with 1× TBS-T, the signal was developed using ECL Western blotting detection reagents (GE Amersham) and visualized on a GE Amersham

shown ($n = 3$ replicates with 100–130 cells counted per replicate for each condition) and significance was determined using the unpaired Student's *t* test (n.s., not significant; ***, $p < 0.0001$). (C) Time-lapse images show HeLa cells expressing GFP-tagged C-terminus control or the *strong* I/F mutant anillin (green) and H2B:mRuby (magenta; to show chromatin; control, $n = 18$; *strong* I/F mut., $n = 7$). Times are from anaphase onset. The scale bar is 10 µm. Cartoon cells on the right show changes in the distribution of anillin (magenta) at the onset of ingression for control vs. the *strong* I/F mutant. (D) Time-lapse images show HeLa cells treated with anillin RNAi and coexpressing RNAi-resistant GFP-tagged full-length control ($n = 15$) or *strong* I/F mutant anillin ($n = 16$; green) and mCherry:tubulin (magenta). The percentages of cells that failed to complete ingression are indicated. Times are from anaphase onset. The scale bar is 10 µm. (E) A cartoon schematic shows how importin binding enhances the RhoA-mediated recruitment of anillin to the equatorial cortex during cytokinesis. (1) RhoA is activated (blue) at anaphase onset and binds to the RBD (magenta), which increases anillin's affinity for importin by causing conformational changes between the RBD and the C2 domain (green). (2) Importin-β (orange) binds to anillin via the C-terminal NLS, which (4) feeds back by stabilizing a conformation that enhances RhoA binding to the RBD. Phospholipids then outcompete importin-β (4) for cooperative binding with RhoA for anillin's enrichment at the equatorial cortex.

Imager 600. Images were converted to 8 bit by ImageJ, and made into figures using Adobe Photoshop and Illustrator (Adobe).

Cosedimentation assays

Microtubules were prepared from lyophilized microtubules (Cytoskeleton) as per manufacturer's instructions in resuspension buffer (15 mM PIPES, 1 mM $MgCl_2$, 20 μM Taxol; Bioshop) at room temperature for 10–15 min with gentle mixing. Aliquots of 45.5 μM were flash-frozen and stored at −80°C, then thawed in a circulating water bath and diluted with resuspension buffer to 9.1 μM. Purified anillin and importin proteins were prespun by centrifugation at 279,000 × *g* for 30 min at room temperature. Cosedimentation reactions were prepared in 200 μl polycarbonate tubes (Beckman Coulter) with 0.5–4 μM of microtubules and 1 μM of purified anillin, or 4 μM of microtubules, 1 μM of purified anillin and 0.2–1.5 μM of purified importin-β, 150 mM NaCl, and BRB80 buffer (80 mM PIPES, pH 6.8, 1 mM EGTA, 1 mM $MgCl_2$) containing 1 mM DTT and 10 μM Taxol. The reactions were kept at room temperature for 15 min, then centrifuged at 279,000 × *g* for 30 min. The supernatants were collected, and pellets were washed and resuspended in BRB80. Sample buffer was added to supernatants and resuspended pellets, which were then run by SDS–PAGE and stained with Coomassie blue. Scanned gels were analyzed in ImageJ to measure the concentration of proteins using line plots to determine pixel intensities that were imported into Excel (Microsoft). After correcting for background, the average intensity was determined. The average amounts of bound anillin (*y*-axis) were plotted against free microtubule concentration (*x*-axis) using GraFit version 7.0.3. The K_d and binding capacity were determined using nonlinear regression ($n = 3$ assays). For the competition assay, after correcting for background, the pixel intensity of anillin in the supernatant was divided by the pixel intensity of anillin in the pellet to obtain a ratio of anillin (S/P) for each concentration of importin-β. Anillin ratios for importin-β concentrations 0.2–1.5 μM were compared with control and data was analyzed using the Student's *t* test ($n = 3$ assays).

Quantification

The breadth and ratio of cortical versus cytosol accumulation for anillin were performed using ImageJ. Maximum intensity Z-projections were generated for each cell, and the breadth was determined using a line scan drawn along the cell cortex. The breadth was determined as the number of pixels above half of the maximum intensity (width of the peak) after subtracting cytosol levels, which was divided by the total number of pixels to give a ratio of breadth to length. To measure the ratio of cortical accumulation versus cytosol, the average intensity was determined in an area drawn around the cortex from one pole to the other. This value was then divided by the average fluorescence intensity from the average of three ROIs in the cytosol. Similar timepoints were selected for anaphase just before ingression based on time from anaphase onset. All data were imported into Excel (Microsoft), where calculations were performed including standard deviations and Student's *t* tests, and to generate graphs. All of the images and graphs were transferred to Illustrator (Adobe) to make figures.

Structural modeling

Structural models were generated using PyMOL version 2.1.1 and transferred to Illustrator (Adobe) to make the figures. Images showing the RBD + C2 domain of anillin were made from PDB ID: 4XH3, and images showing anillin RBD + C2 bound to RhoA-GTP were made from PDB ID: 4XOI (Sun *et al.*, 2015). The amino acids indicated for each structural model correspond to the sequence of human anillin isoform 2 (UniProt entry ID: Q9NQW6-2).

ACKNOWLEDGMENTS

We thank C. Law for help with imaging studies as part of the Centre for Microscopy and Cellular Imaging at Concordia University. We thank C. Brett (Concordia University), I. Cheeseman (Whitehead MIT), and G. Hickson (University of Montreal) for reagents. This work was funded by the Natural Sciences and Engineering Research Council of Canada.

REFERENCES

Basant A, Glotzer M (2018). Spatiotemporal regulation of RhoA during cytokinesis. Curr Biol 28, R570–R580.

Basant A, Lekomtsev S, Tse YC, Zhang D, Longhini KM, Petronczki M, Glotzer M (2015). Aurora B promotes cytokinesis by inducing central-spindlin oligomers that associate with the plasma membrane. Dev Cell 33, 204–215.

Beaudet D, Akhshi T, Phillipp J, Law C, Piekny A (2017). Active Ran regulates anillin function during cytokinesis. Mol Biol Cell 28, 3517–3531.

Bement WM, Benink HA, von Dassow G (2005). A microtubule-dependent zone of active RhoA during cleavage plane specification. J Cell Biol 170, 91–101.

Bringmann H, Cowan CR, Kong J, Hyman A (2007). Let-99, GOA-1/GPA-16, and GPR-1/2 are required for aster-positioned cytokinesis. Curr Biol 17, 185–191.

Bringmann H, Hyman AA (2005). A cytokinesis furrow is positioned by two consecutive signals. Nature 436, 731–734.

Brownlee C, Heald R (2019). Importin α partitioning to the plasma membrane regulates intracellular scaling. Cell 176, 805–815.

Budnar S, Husain KB, Gomez GA, Naghibosadat M, Varma A, Verma S, Hamilton NA, Morris RG, Yap AS (2019). Anillin promotes cell contractility by cyclic resetting of RhoA residence hinetics. Dev Cell 49, 894–906.

Burkard ME, Maciejowski J, Rodriguez-Bravo V, Repka M, Lowery DM, Clauser KR, Zhang C, Shokat KM, Carr SA, Yaffe MB, Jallepalli PV (2009). Plk1 self-organization and priming phosphorylation of HsCYK-4 at the spindle midzone regulate the onset of division in human cells. PLoS Biol 7, e1000111.

Cabernard C, Prehoda KE, Doe CQ (2010). A spindle-independent cleavage furrow positioning pathway. Nature 467, 91–94.

Chang YC, Nalbant P, Birkenfeld J, Chang ZF, Bokoch GM (2008). GEF-H1 couples nocodazole-induced microtubule disassembly to cell contractility via RhoA. Mol Biol Cell 19, 2147–2153.

Chen A, Akhshi TK, Lavoie BD, Wilde A (2015). Importin β2 mediates the spatio-temporal regulation of anillin through a noncanonical nuclear localization signal. J Biol Chem 290, 13500–13509.

Clarke PR, Zhang C (2008). Spatial and temporal coordination of mitosis by Ran GTPase. Nat Rev Mol Cell Biol 9, 464–477.

Dechant R, Glotzer M (2003). Centrosome separation and central spindle assembly act in redundant pathways that regulate microtubule density and trigger cleavage furrow formation. Dev Cell 4, 333–344.

Dehapiot B, Carrière V, Carroll J, Halet G (2013). Polarized Cdc42 activation promotes polar body protrusion and asymmetric division in mouse oocytes. Dev Biol 377, 202–212.

Dehapiot B, Halet G (2013). Ran GTPase promotes oocyte polarization by regulating ERM (Ezrin/Radixin/Moesin) inactivation. Cell Cycle 12, 1672–1678.

Deng M, Suraneni P, Schultz RM, Li R (2007). The Ran GTPase mediates chromatin signalling to control cortical polarity during polar body extrusion in mouse oocytes. Dev Cell 12, 301–308.

El-Amine N, Carim SC, Wernike D, Hickson GRX (2019). Rho-dependent control of the Citron kinase, Sticky, drives midbody ring maturation. Mol Biol Cell 30, 2185–2204.

El-Amine N, Kechad A, Jananji S, Hickson GR (2013). Opposing actions of septins and Sticky on Anillin promote the transition from contractile to midbody ring. J Cell Biol 203, 487–504.

Frenette P, Haines E, Loloyan M, Kinal M, Pakarian P, Piekny A (2012). An anillin-Ect2 complex stabilizes central spindle microtubules at the cortex during cytokinesis. PLoS One 7, e34888.

Green RA, Paluch E, Oegema K (2012). Cytokinesis in animal cells. Annu Rev Cell Dev Biol 28, 29–58.

Kaláb P, Heald R (2008). The RanGTP gradient—a GPS for the mitotic spindle. J Cell Sci 121, 1577–1586.

Kaláb P, Pralle A, Isacoff EY, Heald R, Weis K (2006). Analysis of a RanGTP-regulated gradient in mitotic somatic cells. Nature 440, 697–701.

Kim H, Johnson JM, Lera RF, Brahma S, Burkard ME (2017). Anillin phosphorylation controls timely membrane association and successful cytokinesis. PLoS Genet 13, e1006511.

Kiyomitsu T, Cheeseman IM (2013). Cortical dynein and asymmetric membrane elongation coordinately position the spindle in anaphase. Cell 154, 391–402.
Kotýnková K, Su KC, West SC, Petronczki M (2016). Plasma membrane association but not midzone recruitment of RhoGEF ECT2 is essential for cytokinesis. Cell Rep 17, 2672–2686.
Lakomtsev S, Su KC, Pye VE, Blight K, Sundaramoorthy S, Takaki T, Collinson LM, Cherepanov P, Divecha N, Petronczki M (2012). Centralspindlin links the mitotic spindle to the plasma membrane during cytokinesis. Nature 492, 276–279.
Lammers M, Rose R, Scrima A, Wittinghofer A (2005). The regulation of mDia by autoinhibition and its release by Rho*GTP. EMBO J 24, 4176–4187.
Lewellyn L, Dumont J, Desai A, Oegema K (2010). Analyzing the effects of delaying aster separation on furrow formation during cytokinesis in the *Caenorhabditis elegans* embryo. Mol Biol Cell 21, 50–62.
Li F, Higgs HN (2003). The mouse Formin mDia is a potent actin nucleation factor regulated by autoinhibition. Curr Biol 13, 1335–1340.
Li HY, Zheng Y (2004). Phosphorylation of RCC1 in mitosis is essential for producing high RanGTP concentration on chromosomes and for spindle assembly in mammalian cells. Genes Dev 18, 512–527.
Liu J, Fairn GD, Ceccarelli DF, Sicheri F, Wilde A (2012). Cleavage furrow organization requires PIP(2)-mediated recruitment of anillin. Curr Biol 22, 64–69.
Mangal S, Sacher J, Kim T, Osório DS, Motegi F, Carvalho AX, Oegema K, Zanin E (2018). TPXL-1 activates Aurora A to clear contractile ring components from the polar cortex during cytokinesis. J Cell Biol 217, 837–848.
Mishima M, Kaitna S, Glotzer M (2002). Central spindle assembly and cytokinesis require a kinesin-like protein/RhoGAP complex with microtubule bundling activity. Dev Cell 2, 41–54.
Mishima M, Pavicic V, Grüneberg U, Nigg EA, Glotzer M (2004). Cell cycle regulation of central spindle assembly. Nature 430, 908–913.
Murthy K, Wadsworth P (2008). Dual role for microtubules in regulating cortical contractility during cytokinesis. J Cell Sci 121, 2350–2359.
Oegema K, Savoian MS, Mitchison TJ, Field CM (2000). Functional analysis of a human homologue of the *Drosophila* actin binding protein anillin suggests a role in cytokinesis. J Cell Biol 150, 539–552.
Petronczki M, Glotzer M, Kraut N, Peters JM (2007). Polo-like kinase 1 triggers the initiation of cytokinesis in human cells by promoting recruitment of the RhoGEF Ect2 to the central spindle. Dev Cell 12, 713–725.
Piekny AJ, Glotzer M (2008). Anillin is a scaffold protein that links RhoA, actin, and myosin during cytokinesis. Curr Biol 18, 30–36.
Piekny AJ, Maddox AS (2010). The myriad roles of Anillin during cytokinesis. Sem Cell Dev Biol 21, 881–891.
Piekny A, Werner M, Glotzer M (2005). Cytokinesis: welcome to the Rho zone. Trends Cell Biol 15, 651–658.
Pollard TD, O'Shaughnessy B (2019). Molecular mechanism of cytokinesis. Annu Rev Biochem 88, 661–689.
Rankin KE, Wordeman L (2010). Long astral microtubules uncouple mitotic spindles from the cytokinetic furrow. J Cell Biol 190, 35–43.
Rodrigues NT, Lekomtsev S, Jananji S, Kriston-Vizi J, Hickson GR, Baum B (2015). Kinetochore-localized PP1-Sds22 couples chromosome segregation to polar relaxation. Nature 524, 489–492.
Samwer M, Dehne HJ, Spira F, Kollmar M, Gerlich DW, Urlaub H, Görlich D (2013). The nuclear F-actin interactome of *Xenopus* oocytes reveals an actin-bundling kinesin that is essential for meiotic cytokinesis. EMBO J 32, 1886–1902.
Schenk C, Bringmann H, Hyman AA, Cowan CR (2010). Cortical domain correction repositions the polarity boundary to match the cytokinesis furrow in *C. elegans* embryos. Development 137, 1743–1753.
Sedzinski J, Biro M, Oswald A, Tinevez JY, Salbreux G, Paluch E (2011). Polar actomyosin contractility destabilizes the position of the cytokinetic furrow. Nature 476, 462–466.
Silverman-Gavrila RV, Hales KJ, Wilde A (2008). Anillin-mediated targeting of peanut to pseudocleavage furrows is regulated by the GTPase Ran. Mol Biol Cell 19, 3735–3744.
Solski PA, Wilder RS, Rossman KL, Sondek J, Cox AD, Campbell SL, Der CJ (2004). Requirement for C-terminal sequences in regulation of Ect2 guanine nucleotide exchange specificity and transformation. J Biol Chem 279, 25226–25233.
Somers WG, Saint R (2003). A RhoGEF and Rho family GTPase-activating protein complex links the contractile ring to cortical microtubules at the onset of cytokinesis. Dev Cell 4, 29–39.
Soniat M, Chook YM (2015). Nuclear localization signals for four distinct karyopherin- β nuclear import systems. Biochem J 468, 353–362.
Sun L, Guan R, Lee IJ, Liu Y, Chen M, Wang J, Wu JQ, Chen Z (2015). Mechanistic insights into the anchorage of the contractile ring by anillin and Mid1. Dev Cell 33, 413–426.
Tse YC, Piekny A, Glotzer M (2011). Anillin promotes astral microtubule-directed cortical myosin polarization. Mol Biol Cell 22, 3165–3175.
van Oostende Triplet C, Garcia MJ, Haji Bik H, Beaudet D, Piekny A (2014). Anillin interacts with microtubules and is part of the astral pathway that defines cortical domains. J Cell Sci 127, 3699–3710.
von Dassow G, Verbrugghe KJC, Miller AL, Sider JR, Bement WM (2009). Action at a distance during cytokinesis. J Cell Biol 187, 831–845.
Wagner E, Glotzer M (2016). Local RhoA activation induces cytokinetic furrows independent of spindle position and cell cycle stage. J Cell Biol 213, 641–649.
Weaver LN, Walczak CE (2015). Spatial gradients controlling spindle assembly. Biochem Soc Trans 43, 7–12.
Werner M, Munro E, Glotzer M (2007). Astral signals spatially bias cortical myosin recruitment to break symmetry and promote cytokinesis. Curr Biol 17, 1286–1297.
Wolfe BA, Takaki T, Petronczki M, Glotzer M (2009). Polo-like kinase 1 directs assembly of the HsCyk-4 RhoGAP/Ect2 RhoGEF complex to initiate cleavage furrow formation. PLoS Biol 7, e1000110.
Yüce O, Piekny A, Glotzer M (2005). An ECT2–centralspindlin complex regulates the localization and function of RhoA. J Cell Biol 170, 571–582.
Zanin E, Desai A, Poser I, Toyoda Y, Andree C, Moebius C, Bickle M, Conradt B, Piekny A, Oegema K (2013). A conserved RhoGAP limits M phase contractility and coordinates with microtubule asters to confine RhoA during cytokinesis. Dev Cell 26, 496–510.
Zhao WM, Fang G (2005). MgcRacGAP controls the assembly of the contractile ring and the initiation of cytokinesis. Proc Natl Acad Sci USA 102, 13158–13163.